Dzyaloshinskii-Moriya interaction induced asymmetry in dispersion of magnonic Bloch modes

Hedi Bouloussa, Yves Roussigné, Mohamed Belmeguenai, Andrey Stashkevich, and Salim-Mourad Chérif*
Laboratoire des Sciences des Procédés et des Matériaux, CNRS-UPR 3407, Université Sorbonne Paris Nord, Villetaneuse, 93430, France

Shawn David Pollard and Hyunsoo Yang
Department of Electrical and Computer Engineering, National University of Singapore, 117576, Singapore

(Received 20 January 2020; revised 17 March 2020; accepted 9 June 2020; published 9 July 2020)

We report the results of the experimental investigation of magnonic Bloch modes in the presence of asymmetric dispersion induced by the interfacial Dzyaloshinskii-Moriya interaction by means of Brillouin light-scattering technique. It was realized in a specially designed ultrathin CoFeB/Pt periodic structure consisting of an array of rectangular nanostrips separated by half-etched grooves. The proposed theory based on the coupled mode approach explains the major features observed experimentally, such as Brillouin zone folding and the asymmetry of the magnonic band-gap points in the reciprocal k space.

DOI: 10.1103/PhysRevB.102.014412

I. INTRODUCTION

Magnonics is a rapidly developing field of magnetization dynamics investigating the behavior of spin waves (SWs) in nanopatterned structures seeking to put their unique wave properties to use in important applications related to the vast field of information transport and processing [1–3] that is complementary to mainstream spintronics. Spintronics looks to utilize the inherent "spin" degree of freedom to complement the already successful charge property of the electron used in conventional electronics [4]. In other words, conventional charge currents are replaced with spin currents. Transfer of spin can be implemented in two ways, either via fluxes of electrons with a well-defined spin polarization (spin-polarized current) as in mainstream spintronics or via spin angular momentum carried by collective magnetic-moment precession in SWs (SW spin current) forming the basis of magnon spintronics, or magnonics for short [5]. Substitution of electrons by quasiparticles such as magnons or photons opens up the possibility of the realization of wave-based computing allowing operations with vectors rather than scalar variables, and represents a promising direction for future alternative computing technologies. Introduction of periodicity in magnonic structures radically modifies laws of propagation of SW excitations. Such artificial media typically referred to as magnonic crystals are of great interest for both pure wave physics and highly technologically relevant multifunctional magnonic devices [1]. A magnonic crystal is a magnetic metamaterial and its wave properties arise from geometrical structuring, and not from their composition directly. On the one hand, like other periodic structures, they exhibit such features as band gaps, within which SWs in the form of Bloch modes are not allowed to propagate, and whose major characteristics can be tailor made through *ad hoc* patterning [6]. On the other hand, they can be further tuned by applying external magnetic or electric fields which make these structures extremely flexible and even more attractive for signal and data treatment. Moreover, application of external fields varying in time, as is the case for dynamic magnetic crystals, open up access to magnonic devices whose characteristics can be varied in real time [7]. Although the term magnonic crystal, introduced in 2001 [8], is relatively new, investigations of SWs in periodic structures started much earlier [9,10]. Another promising branch of spintronics opening up the possibility of creation of a generation of energy-saving devices based on spin currents operated without magnetic fields, which currently is a key challenge in this domain, relies on the effects related to spin-orbit coupling (SOC) [11], such as Rashba [12,13] and spin Hall effects [14,15], spin-orbit torques, and Dzyaloshinskii-Moriya Interaction (DMI) [16,17], and is referred to as spin orbitronics. A major trend regarding SOC is that its strength increases for heavier atoms. In terms of solid-state magnetism, DMI can be regarded as an antisymmetric exchange interaction and can only be realized in the absence of inversion symmetry. In this respect, a bilayer composed of a heavy metal (HM) and ferromagnetic metal (FM) seems to be optimal; in this structure, the high SOC efficiency is ensured by the presence of HM atoms while an interface provides the required symmetry reduction, as first suggested by Fert [18]. As a result, the DMI is localized in the close vicinity of the HM/FM interface and thus is referred to as interfacial DMI (iDMI). That is why the role of iDMI can only be pronounced in ultrathin FM structures. Contrary to conventional exchange interaction, DMI favors perpendicular orientation of the neighboring spins, which makes DMI instrumental in stabilizing nanostructures with a preferred chirality [19] such as spin spirals and skyrmions [20–23] or antiskyrmions [24–26]. Importantly, extremely high domain-wall velocities that have been observed in Pt/ferromagnetic are only possible after iDMI-assisted conversion of the inner structure of the domain wall from a Bloch type to a Néel type [27,28].

The interplay between magnonics and the SOC-related iDMI opens access to a wide variety of physical effects and

*cherif@univ-paris13.fr

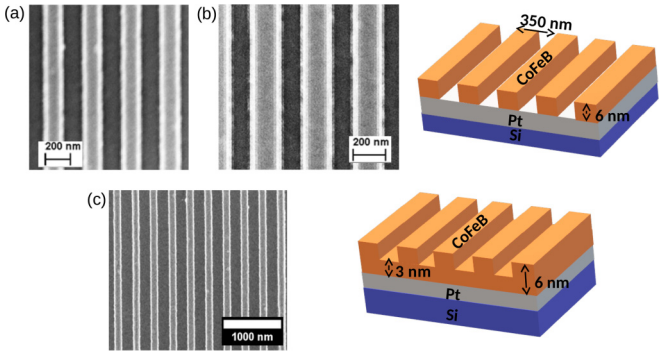

FIG. 1. Patterned areas imaged by scanning electron microscopy: (a) 170-nm-wide strips, (b) 200-nm-wide strips, (c) partially grated layer; the upper sketch corresponds to the separate strips and the lower sketch corresponds to the partially engraved structure.

application-oriented features which is convincingly illustrated by the concept of skyrmion-based dynamic magnonic crystals. Here we report the results of our investigations of another important aspect of SOC-magnonics combination, namely, the DMI-induced asymmetry in the dispersion of magnonic Bloch modes.

II. SAMPLE PREPARATION AND EXPERIMENTS

The initial Pt (6 nm)/$Co_{20}Fe_{60}B_{20}$ (6 nm)/Cu (4 nm) film was deposited on a thermally oxidized Si substrate using d.c. magnetron sputtering in an argon environment. High resolution electron beam lithography with a negative tone resist (MAN-2401) was subsequently used to pattern 0.5 mm $\times$ 0.5 mm arrays of nanostrips with a periodicity p of 350 nm and a variable wire width which depended on the electron dose of the given array. A partially engraved film was created by etching at low power ion milling such that the total CoFeB thickness was decreased by nominally 2–3 nm in the gap region. Following etching, a 4-nm Cu layer was deposited *in situ* to prevent oxidation of the etched regions prior to exposure to atmosphere. The remaining resist was then removed using acetone. A second patterning and etching step was performed to remove any CoFeB from the regions external to the strips. Additionally, an unetched square region was protected during both pattern and etch steps to serve as a reference region. The arrays have been imaged by scanning electron microscopy (SEM). The SEM images as well as sketches of the patterns are displayed in Fig. 1. Additional arrays with completely separated strips, with width $W = 170$ nm and $W = 200$ nm, respectively, were also created as reference samples.

Magnetometry was performed on the initial magnetic film before patterning [see Fig. 2(a)]. The SWs were probed by means of Brillouin light scattering (BLS) technique with a Sandercock tandem spectrometer. The incident and collected light directions determine the wave vector of the propagating excitation in the sample. In the backscattering geometry, the probed propagating waves present a wave vector $k_\theta = \frac{4\pi}{\lambda}\sin\theta$, where λ and θ denote the laser wavelength and its incidence angle with respect to the sample normal, respectively. The experiments were performed in the Damon-Eshbach (DE) geometry: The external field direction is perpendicular to the incident light plane [29,30]. Moreover, the groove direction is parallel to the applied magnetic field.

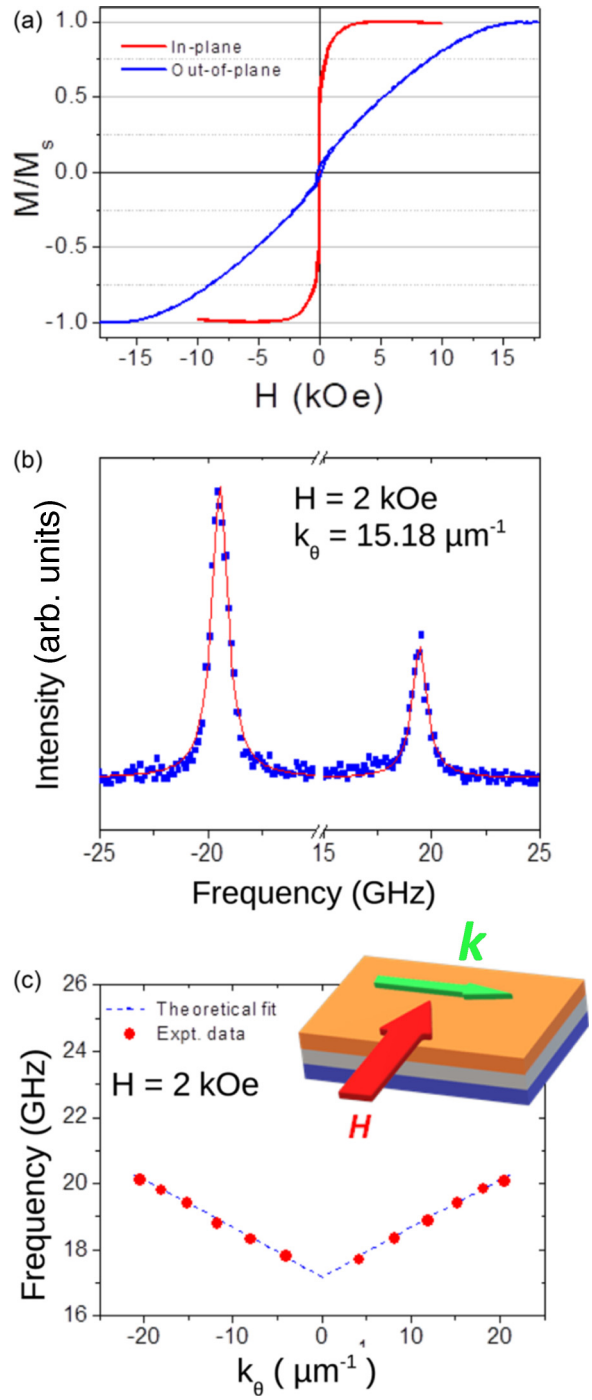

FIG. 2. (a) Hysteresis loops of the 6-nm-thick CoFeB film from vibrating sample magnetometry measurements, (b) typical spectrum for the CoFeB film at H = 2 kOe and $k_\theta = 15.18\ \mu m^{-1}$, (c) dispersion law at H = 2 kOe. The inset represents the sample stack where red and green arrows refer to the applied magnetic field and the spin wave vector directions, respectively.

III. RESULTS AND DISCUSSION

A. Purpose of the study, sample design, and experimental conditions

The goal of this paper is to reveal the influence of the iDMI-induced nonreciprocity on the propagation of the Bloch

collective SW modes in periodic thin-film ferromagnetic structures. However, the design of a structure with a configuration optimized for this particular goal is far from being trivial. This is the result of the compromise between several mutually contradicting criteria as described below.

It should be mentioned that the nonreciprocity of SW Bloch modes can be induced through periodic dynamic coupling [31], also referred to as dynamic pinning [32], which has been observed recently in relatively thick Permalloy (Py) films [33]. In this case, a 30-nm-thick continuous Py film was deposited on a periodic array of 20-nm-thick Ni stripes separated from Py by Cr spacers with a variable thickness (0–50 nm). Theoretical analysis was based on COMSOL numerical simulations. Importantly, the physics behind this nonreciprocity is completely different with respect to our paper. First, this mechanism is critically dependent on the degree of spatial asymmetry of the dynamic magnetization in the DE mode across the FM. This spatial asymmetry becomes more pronounced in thicker FM films. At the same time, it is the interplay of *the asymmetry of the multilayer structure* and *the asymmetry of the DE mode* that is at the bottom of this type of SW nonreciprocity. This means that the SW nonreciprocity becomes more and more pronounced in thicker FM samples, gradually reaching its optimal value which justifies the choice of a 30-nm permalloy layer by the authors of Ref. [33]. This significant increase in the thickness of the FM layer allows us to avoid considerable problems in the realization of magnonic behavior.

First, the pattern period should be compatible with the experimental wave vector range, i.e., the Brillouin zone (BZ) boundary of the periodic structure should be in the vicinity of the middle of the experimental wave vector range $\frac{\pi}{p} \approx 10\ \mu\text{m}^{-1}$ which explains our choice of $p \approx 0.3\ \mu$m. Another point of extreme importance, directly related to the previous issue, is the choice of the optimal thickness t of the structure. On the one hand, its mean value cannot exceed 4–5 nm since the iDMI is a purely interfacial effect and its effective strength scales as $1/t$, as revealed by BLS measurements [34,35]. On the other hand, collective magnetic modes can be evidenced only if the SW coherence length is much larger than the array period, i.e., $\ell_{co} > p$, which implies low microwave losses. The spatial attenuation is described by the imaginary part of the SW vector which is proportional to the imaginary part of the temporal frequency usually referred to as the linewidth of the ferromagnetic resonance δf, the inverse of the SW group velocity v_g playing the role of the coefficient of proportionality. Thus, the coherence length can be estimated by the ratio between the SW group velocity and the frequency line width $\ell_{co} \approx v_g/\delta f$ [36].

The expression of the group velocity of the DE mode in an ultrathin film, like in our case, taking into account the magnetic anisotropy, reads $v_g = \gamma\pi M(4\pi M - H_a)t/\sqrt{H(H + 4\pi M - H_a)}$, where γ, H, M, H_a, t are the gyromagnetic factor, the external field, the saturation magnetization, the perpendicular anisotropy field, and the thickness. As one can see, v_g scales as the film thickness t. In other words, to meet this requirement, the film thickness must be considerably increased which is in an obvious contradiction with the first iDMI related criterion. At the same time, the dependence of v_g on the applied field also suggests using a low value for H which was duly taken into account during our measurements. There exists yet another important aspect in the question of the optimization of the structure thickness. The iDMI is not the only mechanism that is capable of producing nonreciprocity in SW propagation. A non-negligible nonreciprocity can also be induced via asymmetric pinning due to the asymmetry in normal uniaxial interface anisotropy (NUIA), the situation we wish to avoid [37]. Effects from NUIA are more pronounced in thicker samples and therefore suggest a need for thinner samples.

Finally, the type of periodic patterning should also be adapted to the specificity of the investigated phenomena. For entirely separated strips, the dynamic dipolar interstrip coupling field extends only to a distance comparable to the strip thickness. This implies very small interstrip groove widths on the order of several nanometers which is technologically challenging. Thus, the "partially filled grooves" option seems to be far more attractive for the problem at hand, in which case the meander profile with a maximum value of the amplitude of the fundamental spatial harmonic is preferable. All things considered, and taking into account our numerical estimations (see Appendix B), we have chosen to pattern a 6-nm-thick CoFeB film with 2–3-nm-deep grooves to fulfill the requested criteria: for such a film $M = 1300$ emu/cc, $4\pi M - H_a \approx 14$ kOe, $\gamma/2\pi = 3$ GHz/kOe, $\delta f \approx 0.5$ GHz at $H = 0.5$ kOe, and the minimum thickness ("groove" thickness) is about 3 nm, consequently, $\ell_{co} \approx 1.2\ \mu$m.

B. Experimental data and interpretations

We begin our discussion with the experimental data obtained on the reference samples, the native continuous film, and the array of fully separated strips with the FM material entirely removed from the grooves (100% etching) to extract the values of major intrinsic parameters. Finally, we deal with collective magnetic modes influenced by iDMI (partially etched grooves).

The hysteresis loops of the initial 6-nm-thick film are displayed in Fig. 2(a) for both in-plane and out-of-plane applied magnetic fields. From these measurements, we obtain an estimation of the perpendicular saturation field $4\pi M - H_a \approx 14$ kOe (M is the saturation magnetization, H_a is the perpendicular anisotropy field). This estimation is in agreement with that obtained from Brillouin light spectroscopy measurements on the unpatterned film as discussed below.

Typical Brillouin spectrum taken on the continuous film is displayed in Fig. 2(b). One line is observable representing the DE mode. Conversely, a typical Brillouin spectrum obtained on the arrays of fully separated strips exhibits several lines as shown in Fig. 3(a) for the case of the 170-nm-wide strips. The positions of lines deduced from Lorentzian fits as a function of the SW wave vector are shown in Fig. 2(c) for the continuous film and Figs. 3(b) and 3(c) for the 200-nm and 170-nm-wide strips, respectively. The reference samples demonstrate predictable behavior; in the continuous film, SW frequency depends on the wave vector according to the conventional DE pattern while the SW modes on the isolated strip (fully etched grooves) arrays are dispersionless.

The film frequency variations versus the wave vector shown in Fig. 2(c) are fitted using the expression proposed by Kostylev [38]

$$\frac{2\pi f}{\gamma} + \frac{2D_{\text{eff}}}{M}k = \sqrt{\left[H + \frac{2A}{M}k^2 + 4\pi M(1-G)\right]\left(H + \frac{2A}{M}k^2 + 4\pi MG - H_a\right)}, \quad (1)$$

where γ, H, A, M, H_a, k, t, G, D_{eff} are the gyromagnetic factor, the external field, the exchange constant, the saturation magnetization, the perpendicular anisotropy field, the wave vector, the thickness, the averaged demagnetizing factor and the Dzyaloshinskii-Moriya surface constant. For a thin film, this demagnetizing parameter reads $G = \frac{1-\exp(-|kt|)}{|kt|}$. Some parameters were estimated from the literature $\gamma/2\pi = 3$ GHz/kOe, $A = 10^{-6}$ erg/cm, $D_{\text{eff}} = D_s/t$ with $D_s = -10^{-7}$erg/cm(= -1pJ/m) [39]. The magnetization is deduced from magnetometry $M = 1300$ emu/cc. This allowed us to estimate the anisotropy field in the continuous as-grown film. Its fitted value for a 6-nm-thick film is $H_a = 2.5$ kOe which is in good agreement with the estimation from magnetrometry measurements. In a relatively thick 6-nm film, the frequencies for k and $-k$ are very close and consequently the value of the effective constant D_{eff} is very small. As a result, its reliable experimental estimation is not possible at this stage.

The experimental data for the arrays of isolated strips (100% etching) are fitted using expression Eq. (1) with quantized values for the wave vector. Assuming that the continuous film parameters ($\gamma/2\pi = 3$ GHz/kOe, $A = 10^{-6}$ erg/cm, $M = 1300$ emu/cc, $H_a = 2.5$ kOe, $t = 6$ nm) are still valid for the array of isolated strips, we have estimated the strip widths. Interestingly, if, for one reason or another, the effective value iDMI increases and the induced frequency difference for k and $-k$ becomes measurable, such a difference will never take place in isolated strips because standing modes are combinations of counterpropagating waves with the same frequency. Thus the frequency expression Eq. (1) with $D_{\text{eff}} = 0$ is used to fit the strips array frequency variations with respect to the external field by taking $k = \frac{\pi}{W}, \frac{2\pi}{W}, \frac{3\pi}{W}$ [40–43]. Reasonable fits of all the data concerning strip arrays are obtained for $W = 200, 170$ nm [see Figs. 3(b) and 3(c) and Fig. 5 in Appendix B]. The estimated widths are in agreement with those determined from SEM images (see Fig. 1).

For the "magnonic" sample with an intermediate groove depth, several lines can also be observed in the BLS spectra [Fig. 4(a)]. However, conversely to the fully isolated strips, the associated frequencies depend on both absolute value and sign of the wave vector [Fig. 4(b)].

The interpretation of the corresponding experimental data relies on a generalization of Eq. (1) for a periodic thickness. Equation (1) is deduced from the linearized Landau-Lifshitz equation

$$i\left(\frac{\omega}{\gamma} + \frac{2D_{\text{eff}}}{M}k\right)\vec{m} = \vec{M} \times (\vec{h}_d + \vec{h}_e + \vec{h}_a) + \vec{m} \times \vec{H}, \quad (2)$$

where $\vec{m}$ is the dynamic magnetization, $\vec{h}_d$, $\vec{h}_e$, $\vec{h}_a$ are the dynamic demagnetizing, exchange, and anisotropy fields. We denote $\vec{u}_z$ the unit vector parallel to the applied field, $\vec{u}_x$ the unit vector parallel to the wave vector, and $\vec{u}_y$ the normal to the sample. The dynamic fields read $\vec{h}_d = -4\pi((1-G)m_x\vec{u}_x + Gm_y\vec{u}_y)$, $\vec{h}_e = -\frac{2A}{M}k^2\vec{m}$, $\vec{h}_a = \frac{2K}{M}m_y\vec{u}_y$, where the anisotropy constant K is deduced from the static anisotropy field H_a by the relation $K = \frac{1}{2}MH_a$.

For the sake of simplicity and without losing generality, we assume a sinusoidal variation of thickness $t = t_0 + t_1\cos(qx)$. This means that the three major physical parameters, namely, the demagnetizing factor, the anisotropy, and DMI constants, will be modulated accordingly: $G = G(|k|t_0) + |k|t_1\cos(qx)\frac{\partial G}{\partial u}$ with $G(u) = u^{-1}[1-\exp(-u)]$,

$K = K(t_0) + t_1\cos(qx)\frac{\partial K}{\partial t}$ with $K(t) = K_v + K_s t^{-1}$, and $D_{\text{eff}} = D_{\text{eff}}(t_0) + t_1\cos(qx)\frac{\partial D_{\text{eff}}}{\partial t}$ with $D_{\text{eff}} = D_s t^{-1}$.

Consequently $\exp(ikx)$, $\exp[i(k-q)x]$ and $\exp[i(k+q)x]$ waves will be coupled (see calculation details in Appendix A) via these three mechanisms. Strictly speaking, higher harmonics in the Fourier series expansion of the meander etching profile should also be taken into account. This means that the SW with a wave vector k will be coupled to all multiple harmonics $k + nq$ (n is an integer), creating an infinite set of harmonic contributions. In classic wave science, such a solution is known as Floquet's theorem [44]. In solid-state physics, wave propagation in periodic structures is interpreted in terms of BZ folding. In our particular case of a meander-type profile, the amplitudes of higher spatial harmonics are appreciably smaller than that of the fundamental one which makes coupling through them considerably weaker. This justifies our supposition that the actual meander profile can be replaced with its fundamental harmonic without loss of generality. Importantly, taking into account of the coupling with only the nearest $k+q$ and $k-q$ spatial harmonics is sufficient to explain the major feature observed experimentally, namely the appearance of two additional peaks in the BLS spectra [see Fig. 4(a)]. The main peak (No. 1) corresponds to the $\exp(ikx)$ wave. The satellite peaks corresponding to $\exp[i(k-q)x]$ (No. 2) and $\exp[i(k+q)x]$ (No. 3) waves are not visible if they are too close or too far from the main line: too closely, they disappear in the main peak, too far the coupling is not efficient to make the satellite peaks visible. The calculated frequencies fit the measured values for the following parameters: $M = 1300$ emu/cc, $A = 10^{-6}$ erg/cm, $\gamma/2\pi = 3$ GHz/kOe, $K_v = 1.625$ Merg/cc (four parameters identical to those for the initial film, K_v corresponds to $H_a = 2.5$ kOe), $D_s = -10^{-7}$ erg/cm (i.e., $= -1$pJ/m), and $q = 18 \times 10^4$ cm^{-1}. The fitting q value corresponds to a periodicity $p = \frac{2\pi}{q} = 350$ nm. Moreover, the fitting value for t_0 is 3.3 nm.

Contrary to the results obtained on the continuous film or the separated strips, a number of pronounced iDMI related asymmetries in SW spectra can be observed. On the one hand, all effects originating from the iDMI become more pronounced in thinner FM films. It is not surprising that the asymmetry of the main dispersion branch in a magnonic

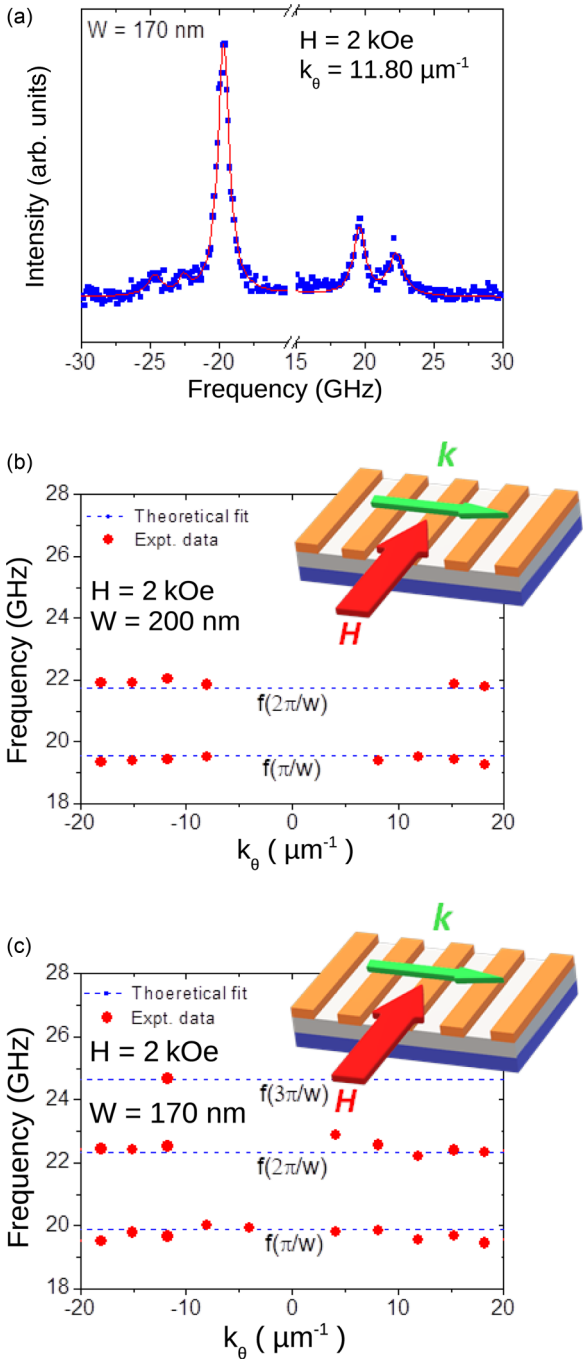

FIG. 3. (a) Brillouin light scattering spectrum for the 170-wide-strip array. Dispersion laws for the $W = 200$ nm (b) and $W = 170$ nm (c) strip arrays at H = 2 kOe.

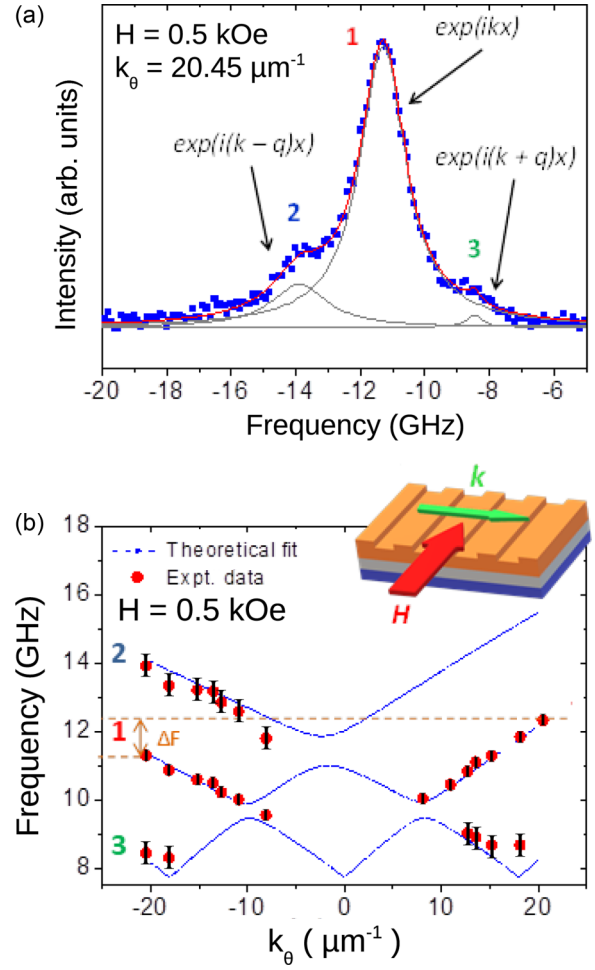

FIG. 4. (a) Stokes side of the spectrum for the partially etched layer at H = 0.5 kOe and $k_\theta = 20.45\ \mu\text{m}^{-1}$, (b) dispersion law at H = 0.5 kOe, ΔF indicates the maximal observed frequency asymmetry on the main peak, error bars for the main line indicate the frequencies are measured within ±0.15 GHz, errors bars for the satellite lines indicate the frequencies are measured within ±0.3 GHz because their positions depend on the precision on the main line position.

structure (8 GHz $< f <$ 12 GHz, $0 < k <$22 μm^{-1}) with an effective thickness of 3.3 nm is clearly observable while that in a 6-nm-thick continuous film is not. The fact that it is the effective thickness that appears in the numerical simulations successfully fitting the experimental data is direct proof of the magnonic nature of the wave process. Importantly, this best-fitting thickness is equal to $t_{\text{eff}} = 3.3$ nm, which is far from the value prompted by simple intuition for the case of meander patterning, which suggests the value of 4.5 nm, i.e., the average of two thicknesses. Moreover, in the patterned sample, there exist iDMI-related effects that are only possible in a magnonic structure. First, this applies to the upper dispersion branch (12 GHz $< f <$ 14 GHz) directly resulting from BZ folding. Actually, it corresponds to the 22 $\mu\text{m}^{-1} < k <$44 μm^{-1} range and is shifted due to folding to the $0 < k <$22 μm^{-1} one which is covered by the BLS technique. This doubles the iDMI-induced effect on the frequency. Indeed, this effect is proportional to the effective wave vector. Another promising effect is related to the shift of the BZ edges in the reciprocal k space (band-gap points). It is a result of a trade-off between the conventional dipolar DE *sign-independent dispersion* and the *sign-dependent* iDMI induced dispersion. As with all iDMI-related effects, this asymmetry becomes more pronounced in thinner films. Importantly, this dependence on the film thickness is highly nonlinear and there exists a critical thickness below which no intersection of the dispersion branches takes place, excluding the possibility of the band-gap effects. The realizability of this characteristic feature is unique to the iDMI-induced SW nonreciprocity.

In any case, in thin FM films under 3 nm, the shift of the band-gap points is very sensitive to the magnitude of the iDMI constant. Thus, in our magnonic sample having an effective thickness of 3.3 nm, the asymmetry of the band-gap points $\frac{k_- - k_+}{k_{av}}$ in the reciprocal k space is 17%, while the asymmetry of the temporal frequencies is only about 3.6%, as can be observed from the positions of the crossings in Fig. 4(b).

IV. CONCLUSION

We have studied the behavior of DE Bloch modes in an ultrathin periodic CoFeB/Pt structures designed *ad hoc* to ensure simultaneous realization of both periodicity-related magnonic features and the pronounced iDMI-related nonreciprocity by means of BLS technique. This has been achieved in an array of rectangular strips with a period of 350 nm separated by half-etched grooves acting as a magnonic SW waveguide with an effective thickness of 3.3 nm. In particular, it was shown that the asymmetry of the magnonic band-gap points in the reciprocal k space can be several times more pronounced than the conventional asymmetry of the temporal frequencies. Moreover, the observed values of the iDMI-induced Stokes/anti-Stokes frequency asymmetry were doubled due to BZ folding, leading to doubling of the effective range of SW wave numbers. In other words, the already non-negligible SW nonreciprocity in a CoFeB layer with an effective magnetic thickness of 3.3 nm was further enhanced through magnonic features such as BZ folding. The observed features were explained both qualitatively and numerically on the basis of an approximate theory based on the classical coupled-wave formalism with the values of major parameters describing the structure extracted from characterization of the reference samples (a continuous film and a fully etched array of uncoupled strips).

ACKNOWLEDGMENTS

This work has been supported by the Conseil Régional d'Île-de-France through the DIM NanoK (Bidul project, convention No. 1763, 2016 NANO-K DIM programme), SpOT-LITE program (A*STAR Grant No. A18A6b0057) through RIE 2020 funds, and by the USPC-NUS alliance grant (Imansa project, 2016-01R/USPC-NUS).

APPENDIX A: FREQUENCY CALCULATION FOR A OSCILLATORY THICKNESS

In the case of a layer with a uniform thickness, Eq. (2) yields

$$i\left(\frac{\omega}{\gamma}+\frac{2D_{\text{eff}}}{M}k\right)m_x^{(k)}=\left(H+\frac{2A}{M}k^2+4\pi MG-\frac{2K}{M}\right)m_y^{(k)}, \tag{A1}$$

$$i\left(\frac{\omega}{\gamma}+\frac{2D_{\text{eff}}}{M}k\right)m_y^{(k)}=-\left[H+\frac{2A}{M}k^2+4\pi M(1-G)\right]m_x^{(k)}. \tag{A2}$$

Equating the determinant associated to Eqs. (A1) and (A2) to 0 yields Eq. (1). Let us denote $G_0^{(k)}=G(|k|t_0)$, $G_1^{(k)}=t_1\frac{\partial G(|k|t)}{\partial t}(t_0)$, $G_0^{(k\pm q)}=G(|k\pm q|t_0)$, $G_1^{(k\pm q)}=t_1\frac{\partial G(|k\pm q|t)}{\partial t}(t_0)$, $K_0=K(t_0)$, $K_1=t_1\frac{\partial K}{\partial t}(t_0)$, $D_0=D_{\text{eff}}(t_0)$, $D_1=t_1\frac{\partial D_{\text{eff}}}{\partial t}(t_0)$. Equations (A1) and (A2) are replaced with

$$\begin{aligned}&i\left(\frac{\omega}{\gamma}+\frac{2D_0}{M}k\right)m_x^{(k)}+i\left[\frac{D_1}{M}(k-q)\right]m_x^{(k-q)}+i\left[\frac{D_1}{M}(k+q)\right]m_x^{(k+q)}\\&\quad=\left(H+\frac{2A}{M}k^2+4\pi MG_0^{(k)}-\frac{2K_0}{M}\right)m_y^{(k)}+\left(2\pi MG_1^{(k-q)}-\frac{K_1}{M}\right)m_y^{(k-q)}+\left(2\pi MG_1^{(k+q)}-\frac{K_1}{M}\right)m_y^{(k+q)}\end{aligned} \tag{A3}$$

$$\begin{aligned}&i\left(\frac{\omega}{\gamma}+\frac{2D_0}{M}k\right)m_y^{(k)}+i\left[\frac{D_1}{M}(k-q)\right]m_y^{(k-q)}+i\left(\frac{D_1}{M}(k+q)\right)m_y^{(k+q)}\\&\quad=-\left[H+\frac{2A}{M}k^2+4\pi M\left(1-G_0^{(k)}\right)\right]m_x^{(k)}+\left(2\pi MG_1^{(k-q)}\right)m_x^{(k-q)}+\left(2\pi MG_1^{(k+q)}\right)m_x^{(k+q)}\end{aligned} \tag{A4}$$

$$\begin{aligned}&i\left[\frac{\omega}{\gamma}+\frac{2D_0}{M}(k-q)\right]m_x^{(k-q)}+i\left(\frac{D_1}{M}k\right)m_x^{(k)}+i\left[\frac{D_1}{M}(k+q)\right]m_x^{(k+q)}\\&\quad=\left[H+\frac{2A}{M}(k-q)^2+4\pi MG_0^{(k-q)}-\frac{2K_0}{M}\right]m_y^{(k-q)}+\left(2\pi MG_1^{(k)}-\frac{K_1}{M}\right)m_y^{(k)}+\left(2\pi MG_1^{(k+q)}-\frac{K_1}{M}\right)m_y^{(k+q)}\end{aligned} \tag{A5}$$

$$\begin{aligned}&i\left[\frac{\omega}{\gamma}+\frac{2D_0}{M}(k-q)\right]m_y^{(k-q)}+i\left(\frac{D_1}{M}k\right)m_y^{(k)}+i\left[\frac{D_1}{M}(k+q)\right]m_y^{(k+q)}\\&\quad=-\left[H+\frac{2A}{M}(k-q)^2+4\pi M\left(1-G_0^{(k-q)}\right)\right]m_x^{(k-q)}+\left(2\pi MG_1^{(k)}\right)m_x^{(k)}+\left(2\pi MG_1^{(k+q)}\right)m_x^{(k+q)}\end{aligned} \tag{A6}$$

$$i\left[\frac{\omega}{\gamma}+\frac{2D_0}{M}(k+q)\right]m_x^{(k+q)}+i\left(\frac{D_1}{M}k\right)m_x^{(k)}+i\left[\frac{D_1}{M}(k-q)\right]m_x^{(k-q)}$$

$$=\left[H+\frac{2A}{M}(k+q)^2+4\pi MG_0^{(k+q)}-\frac{2K_0}{M}\right]m_y^{(k+q)}+\left(2\pi MG_1^{(k)}-\frac{K_1}{M}\right)m_y^{(k)}+\left(2\pi MG_1^{(k-q)}-\frac{K_1}{M}\right)m_y^{(k-q)} \quad \text{(A7)}$$

$$i\left[\frac{\omega}{\gamma}+\frac{2D_0}{M}(k+q)\right]m_y^{(k+q)}+i\left[\frac{D_1}{M}k\right)m_y^{(k)}+i\left(\frac{D_1}{M}(k-q)\right)\Big]m_y^{(k-q)}$$

$$=-\left[H+\frac{2A}{M}(k+q)^2+4\pi M\left(1-G_0^{(k+q)}\right)\right]m_x^{(k+q)}+\left(2\pi MG_1^{(k)}\right)m_x^{(k)}+\left(2\pi MG_1^{(k-q)}\right)m_x^{(k-q)} \quad \text{(A8)}$$

Equating the determinant associated to Eqs. (A3)–(A8) to 0 yields the three eigenfrequencies for coupled waves $\exp(ikx)$, $\exp[i(k-q)x]$ and $\exp[i(k+q)x]$.

APPENDIX B: EXPERIMENTAL RESULTS AND FITTING CURVES FOR THE FREQUENCY VARIATION VERSUS THE APPLIED FIELD

To check the values of the quantized vector in the case of separated strips, we have compared the calculated frequencies with the observed discrete modes frequencies for several applied fields (see Fig. 5).

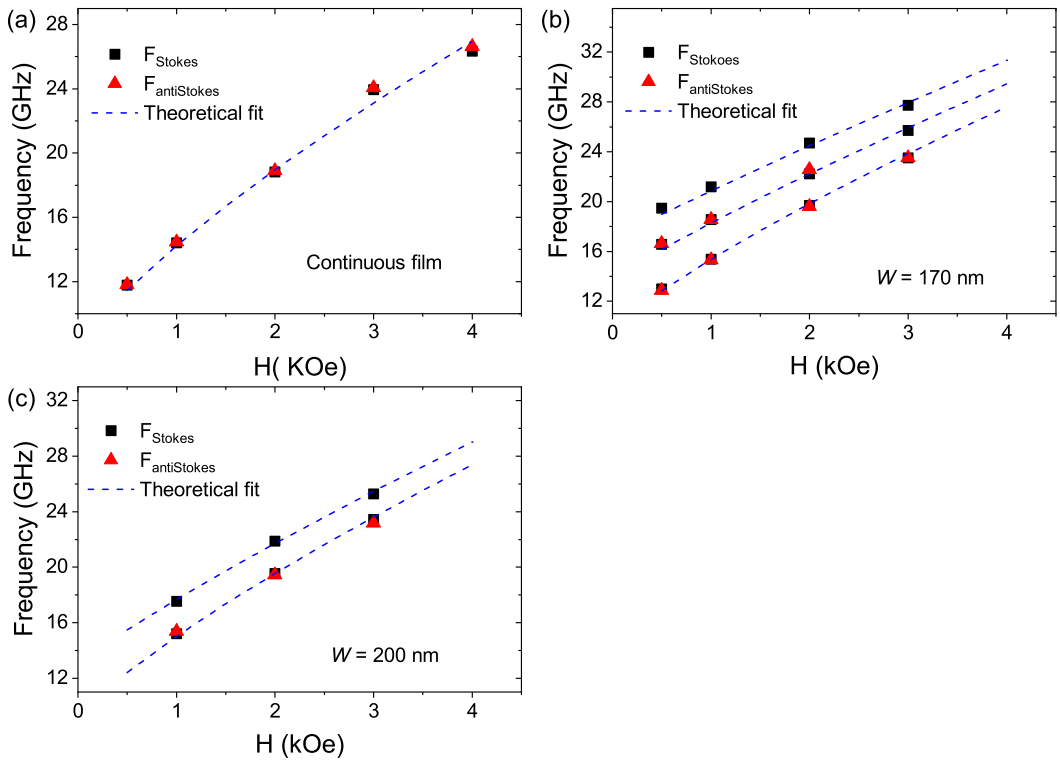

FIG. 5. (a) Frequency dependence on the applied magnetic field for the continuous film, (b) the 170-nm-wide strips and (c) the 200-nm-wide strips. The symbols refer to the experimental data and the dashed lines to the theoretical fits.

[1] A. V. Chumak and H. Schultheiss, Magnonics: Spin waves connecting charges, spins and photons, J. Phys. D **50**, 300201 (2017).

[2] C. S. Davies, A. Francis, A. V. Sadovnikov, S. V. Chertopalov, M. T. Bryan, S. V. Grishin, D. A. Allwood, Y. P. Sharaevskii, S. A. Nikitov, and V. V. Kruglyak, Towards graded-index magnonics: Steering spin waves in magnonic networks, Phys. Rev. B **92**, 020408(R) (2015).

[3] F. Garcia-Sanchez, P. Borys, R. Soucaille, J.-P. Adam, R. L. Stamps, and J.-V. Kim, Narrow Magnonic Waveguides Based on Domain Walls, Phys. Rev. Lett. **114**, 247206 (2015).

[4] A. Fert, Nobel lecture: Origin, development, and future of spintronics, Rev. Mod. Phys. **80**, 1517 (2008).

[5] A. V. Chumak, V. I. Vasyuchka, A. A. Serga, and B. Hillebrands, Magnon spintronics, Nat. Phys. **11**, 453 (2015).

[6] M. Krawczyk and D. Grundler, Review and prospects of magnonic crystals and devices with reprogrammable band structure, J. Phys.: Condens. Matter **26**, 123202 (2014).

[7] A. V. Chumak, T. Neumann, A. A. Serga, B. Hillebrands, and M. P. Kostylev, A current-controlled, dynamic magnonic crystal, J. Phys. D **42**, 205005 (2009).

[8] S. A. Nikitov, P. Tailhades, and C. S. Tsai, Spin waves in periodic magnetic structures–magnonic crystals, J. Magn. Magn. Mater. **236**, 320 (2001).

[9] C. G. Sykes, J. D. Adam, and J. H. Collins, Magnetostatic wave propagation in a periodic structure, Appl. Phys. Lett. **29**, 388 (1976).

[10] J. Gouzerh, A. A. Stashkevich, N. G. Kovshikov, V. V. Matyushev, and J. M. Desvignes, Reflection of magnetostatic waves from a laser-annealed grating in a garnet film, J. Magn. Magn. Mater. **101**, 189 (1991).

[11] A. Soumyanarayanan, N. Reyren, A. Fert, and C. Panagopoulos, Emergent phenomena induced by spin–orbit coupling at surfaces and interfaces, Nature **539**, 509 (2016).

[12] Y. A. Bychkov and É. I. Rashba, Properties of a 2d electron gas with lifted spectral degeneracy, JETP Lett. **39**, 78 (1984).

[13] A. Manchon, H. C. Koo, J. Nitta, S. M. Frolov, and R. A. Duine, New perspectives for rashba spin–orbit coupling, Nat. Mater. **14**, 871 (2015).

[14] M. I. Dyakonov and V. I. Perel, Current-induced spin orientation of electrons in semiconductors, Phys. Lett. A **35**, 459 (1971).

[15] J. Sinova, S. O. Valenzuela, J. Wunderlich, C. H. Back, and T. Jungwirth, Spin hall effects, Rev. Mod. Phys. **87**, 1213 (2015).

[16] I. Dzyaloshinsky, A thermodynamic theory of "weak" ferromagnetism of antiferromagnetics, J. Phys. Chem. Solids **4**, 241 (1958).

[17] T. Moriya, New Mechanism of Anisotropic Superexchange Interaction, Phys. Rev. Lett. **4**, 228 (1960).

[18] A. Fert, Magnetic and transport properties of metallic multilayers, in *Materials Science Forum* (Trans Tech Publications, Switzerland, 1990), Vol. 59, pp. 439–480.

[19] A. Thiaville, S. Rohart, É. Jué, V. Cros, and A. Fert, Dynamics of Dzyaloshinskii domain walls in ultrathin magnetic films, Europhys. Lett. **100**, 57002 (2012).

[20] S. D. Yi, S. Onoda, N. Nagaosa, and J. H. Han, Skyrmions and anomalous Hall effect in a Dzyaloshinskii-Moriya spiral magnet, Phys. Rev. B **80**, 054416 (2009).

[21] A. Fert, V. Cros, and J. Sampaio, Skyrmions on the track, Nat. Nanotechnol. **8**, 152 (2013).

[22] O. Boulle, J. Vogel, H. Yang, S. Pizzini, D. de Souza Chaves, A. Locatelli, T. O. Menteş, A. Sala, L. D. Buda-Prejbeanu, O. Klein *et al.*, Room-temperature chiral magnetic skyrmions in ultrathin magnetic nanostructures, Nat. Nanotechnol. **11**, 449 (2016).

[23] S. Woo, K. Litzius, B. Krüger, M.-Y. Im, L. Caretta, K. Richter, M. Mann, A. Krone, R. M. Reeve, M. Weigand *et al.*, Observation of room-temperature magnetic skyrmions and their current-driven dynamics in ultrathin metallic ferromagnets, Nat. Mater. **15**, 501 (2016).

[24] L. Camosi, S. Rohart, O. Fruchart, S. Pizzini, M. Belmeguenai, Y. Roussigné, A. Stashkevich, S. M. Chérif, L. Ranno, M. de Santis, and J. Vogel, Anisotropic Dzyaloshinskii-Moriya interaction in ultrathin epitaxial Au/Co/W (110), Phys. Rev. B **95**, 214422 (2017).

[25] S. Huang, C. Zhou, G. Chen, H. Shen, A. K. Schmid, K. Liu, and Y. Wu, Stabilization and current-induced motion of antiskyrmion in the presence of anisotropic Dzyaloshinskii-Moriya interaction, Phys. Rev. B **96**, 144412 (2017).

[26] M. Hoffmann, B. Zimmermann, G. P. Muller, D. Schurhoff, N. S. Kiselev, C. Melcher, and S. Blugel, Antiskyrmions stabilized at interfaces by anisotropic Dzyaloshinskii-Moriya interactions, Nat. Commun. **8**, 308 (2017).

[27] K.-S. Ryu, L. Thomas, S.-H. Yang, and S. Parkin, Chiral spin torque at magnetic domain walls, Nat. Nanotechnol. **8**, 527 (2013).

[28] K.-S. Ryu, S.-H. Yang, L. Thomas, and S. S. P. Parkin, Chiral spin torque arising from proximity-induced magnetization, Nat. Commun. **5**, 3910 (2014).

[29] S. O. Demokritov and E. Tsymbal, Light scattering from spin waves in thin films and layered systems, J. Phys.: Condens. Matter **6**, 7145 (1994).

[30] F. Zighem, Y. Roussigné, S. M. Chérif, and P. Moch, Spin wave modeling in arrays of ferromagnetic thin stripes: Application to Brillouin light scattering in permalloy, J. Phys.: Condens. Matter **19**, 176220 (2007).

[31] S. Tacchi, G. Gubbiotti, M. Madami, and G. Carlotti, Brillouin light scattering studies of 2d magnonic crystals, J. Phys.: Condens. Matter **29**, 073001 (2017).

[32] M. Kostylev, A. Stashkevich, A. O. Adeyeye, C. Shakespeare, N. Kostylev, N. Ross, K. Kennewell, R. Magaraggia, Y. Roussigné, and R. L. Stamps, Magnetization pinning in conducting films demonstrated using broadband ferromagnetic resonance, J. Appl. Phys. **108**, 103914 (2010).

[33] M. Mruczkiewicz, P. Graczyk, P. Lupo, A. O. Adeyeye, G. Gubbiotti, and M. Krawczyk, Spin-wave nonreciprocity and magnonic band structure in a thin permalloy film induced by dynamical coupling with an array of Ni stripes, Phys. Rev. B **96**, 104411 (2017).

[34] J. Cho, N.-H. Kim, S. Lee, J.-S. Kim, R. Lavrijsen, A. Solignac, Y. Yin, D.-S. Han, N. J. J. Van Hoof, H. J. M. Swagten, B. Koopmans, and C.-Y. You, Thickness dependence of the interfacial Dzyaloshinskii-Moriya interaction in inversion symmetry broken systems, Nat. Commun. **6**, 7635 (2015).

[35] M. Belmeguenai, M. S. Gabor, Y. Roussigné, A. Stashkevich, S. M. Chérif, F. Zighem, and C. Tiusan, Brillouin light scattering investigation of the thickness dependence of Dzyaloshinskii-Moriya interaction in $Co_{0.5}Fe_{0.5}$ ultrathin films, Phys. Rev. B **93**, 174407 (2016).

[36] H. Bouloussa, J. Yu, Y. Roussigné, M. Belmeguenai, A. Stashkevitch, H. Yang, and S. M. Chérif, Brillouin light scattering investigation of interfacial Dzyaloshinskii-Moriya interaction in ultrathin Co/Pt nanostripe arrays, J. Phys. D **51**, 225005 (2018).

[37] A. A. Stashkevich, M. Belmeguenai, Y. Roussigné, S. M. Chérif, M. Kostylev, M. Gabor, D. Lacour, C. Tiusan, and M.

Hehn, Non-reciprocity of spin wave propagation induced by the interface Dzyaloshinskii-Moriya interaction in Py/Pt film structures, Phys. Rev. B **91**, 214409 (2015).

[38] M. Kostylev, Interface boundary conditions for dynamic magnetization and spin wave dynamics in a ferromagnetic layer with the interface Dzyaloshinskii-Moriya interaction, J. Appl. Phys. **115**, 233902 (2014).

[39] K. Di, V. L. Zhang, H. S. Lim, S. C. Ng, M. H. Kuok, X. Qiu, and H. Yang, Asymmetric spin-wave dispersion due to Dzyaloshinskii-Moriya interaction in an ultrathin Pt/CoFebB film, Appl. Phys. Lett. **106**, 052403 (2015).

[40] J. Jorzick, S. O. Demokritov, C. Mathieu, B. Hillebrands, B. Bartenlian, C. Chappert, F. Rousseaux, and A. N. Slavin, Brillouin light scattering from quantized spin waves in micron-size magnetic wires, Phys. Rev. B **60**, 15194 (1999).

[41] Y. Roussigné, S. M. Chérif, C. Dugautier, and P. Moch, Experimental and theoretical study of quantized spin-wave modes in micrometer-size permalloy wires, Phys. Rev. B **63**, 134429 (2001).

[42] Y. Roussigné, S. M. Chérif, and P. Moch, Spin waves calculations in magnetic stripes, J. Magn. Magn. Mater. **263**, 289 (2003).

[43] K. Y. Guslienko and A. N. Slavin, Magnetostatic Green's functions for the description of spin waves in finite rectangular magnetic dots and stripes, J. Magn. Magn. Mater. **323**, 2418 (2011).

[44] P. M. Morse and H. Feshbach, *Methods of Theoretical Physics*, (McGraw-Hill, New York, 1953), Vol. 1.